

# PHOTONICS Research

## All-optical neuromorphic binary convolution with a spiking VCSEL neuron for image gradient magnitudes

YAHUI ZHANG,<sup>1,2</sup> JOSHUA ROBERTSON,<sup>1</sup> SHUIYING XIANG,<sup>2,\*</sup> MATĚJ HEJDA,<sup>1</sup> JULIÁN BUENO,<sup>1</sup> AND ANTONIO HURTADO<sup>1,3</sup>

<sup>1</sup>Institute of Photonics, SUPA Department of Physics, University of Strathclyde, Glasgow G1 1RD, UK

<sup>2</sup>State Key Laboratory of Integrated Service Networks, Xidian University, Xi'an 710071, China

<sup>3</sup>e-mail: antonio.hurtado@strath.ac.uk

\*Corresponding author: jxxy@126.com

Received 9 October 2020; revised 2 February 2021; accepted 18 February 2021; posted 19 February 2021 (Doc. ID 412141); published 14 April 2021

All-optical binary convolution with a photonic spiking vertical-cavity surface-emitting laser (VCSEL) neuron is proposed and demonstrated experimentally for the first time, to the best of our knowledge. Optical inputs, extracted from digital images and temporally encoded using rectangular pulses, are injected in the VCSEL neuron, which delivers the convolution result in the number of fast (<100 ps long) spikes fired. Experimental and numerical results show that binary convolution is achieved successfully with a single spiking VCSEL neuron and that all-optical binary convolution can be used to calculate image gradient magnitudes to detect edge features and separate vertical and horizontal components in source images. We also show that this all-optical spiking binary convolution system is robust to noise and can operate with high-resolution images. Additionally, the proposed system offers important advantages such as ultrafast speed, high-energy efficiency, and simple hardware implementation, highlighting the potentials of spiking photonic VCSEL neurons for high-speed neuromorphic image processing systems and future photonic spiking convolutional neural networks. © 2021 Chinese Laser Press

<https://doi.org/10.1364/PRJ.412141>

### 1. INTRODUCTION

Convolutional neural networks (CNNs) have seen tremendous success in many applications, such as speech and image recognition [1,2], computer vision [3], and document analysis [4]. However, CNN-based systems are computationally expensive due to their complicated architectures and the large number of parameters they rely on. CNNs therefore typically require the implementation of multicore central processing units and graphics processing units to compensate for the rather high computational expense [5,6]. This makes CNN architectures often unsuitable for smaller devices like phones and smart cameras, where power and speed have strict limitations. To address these drawbacks, the optimization and discovery of new high-speed and low power consumption platforms for CNNs are urgently required. For the optimization of CNNs, binary CNNs, which are simple, efficient, and accurate approximations of complete CNNs, can be introduced [7–9]. In binary CNNs, the weights given to the inputs of each convolutional layer are approximated with binary values [7]. Therefore, binary CNNs boast 58× faster convolutional operations and 32× less memory requirements than traditional CNNs [7].

Several optimized binary versions of CNNs have been proposed for training processes and image classification tasks [7,10,11]. However, beyond the optimization of CNNs, a new platform offering high speed and low power consumption remains highly desirable.

Photonics is considered a highly promising candidate for future neural network implementations given the unique advantages it provides such as high speed, wide bandwidth, and low power consumption [12–21]. Photonics-based CNNs have therefore been proposed in order to increase the speed of convolutional operations [18–21]. A photonic CNN accelerator was proposed based on silicon photonic micro-ring weighting banks [18]. The full system design offers more than three orders of magnitude improvement in execution time, and its optical core potentially offers more than five orders of magnitude improvement compared to state-of-the-art electronic counterparts [18]. Xu *et al.* also proposed high-accuracy optical convolution unit architecture based on acousto-optical modulator arrays, where the optical convolution unit was shown to perform well on inferences of typical CNN tasks [20]. However, the size of the system is based on the size of the kernel utilized in these emerging works on photonic CNNs.

In this work, we propose an all-optical binary convolution system using a single vertical-cavity surface-emitting laser (VCSEL) operating as a spiking optical neuron, hence, dramatically reducing hardware requirements. In our approach, temporal encoding is used instead of spatial encoding, thus crucially helping to reduce (optical) hardware complexity. In our all-optical binary convolution technique, results are represented by the number of fast (<100 ps long) spiking responses delivered by the optical spiking VCSEL neuron. This has unique advantages in terms of robustness to noise and high precision. Additionally, VCSELs have unique inherent advantages, such as high-energy efficiency, high-speed modulation capability, low bias currents, easy packaging, and highly integrable structures [22,23]. In particular, VCSELs have demonstrated the ability to generate fast spiking dynamics analogous to those of biological neurons known for their robustness to input noise [24–29]. The controlled activation, inhibition, and communication of these neuronal dynamics has been demonstrated, and recently a single VCSEL device was used to perform spiking pattern recognition and rate coding [24–31]. Thus, photonic spiking VCSELs make suitable candidates for a new future photonic platform for ultrafast energy efficient spiking CNNs.

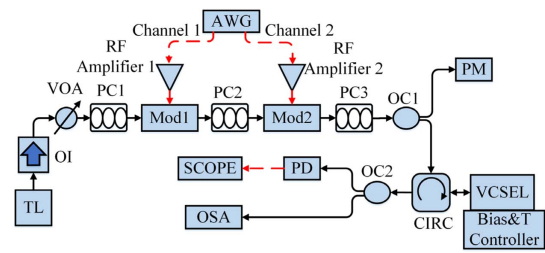
In this work, we use a VCSEL-based photonic approach for binary convolution to demonstrate image gradient magnitude calculation. This delivers an essential portion of the image edge detection functionality used by computer vision and image recognition systems. Here, a single VCSEL system is developed to solely perform a convolution operation; hence, no VCSEL-based CNN architecture, capable of providing learning and classification capabilities, is discussed in this work. The rest of the paper is organized as follows. Section 2 is devoted to the experimental setup of this work for the demonstration of all-optical binary convolution with a spiking VCSEL neuron and the theoretical model used to predict the response of the system. In Section 3, convolutional results are analyzed before the full calculation of image gradient magnitudes is performed both experimentally and theoretically. Finally, Section 4 summarizes the conclusions of this work.

## 2. EXPERIMENTAL SETUP AND THEORETICAL MODEL

We present here the experimental arrangement and theoretical model of the all-optical binary convolution system based on a photonic spiking VCSEL neuron. In this work, we set a source digital image and a kernel as the two inputs of the convolution system. The value of any one pixel in the source image or kernel is limited to 0 or 1.

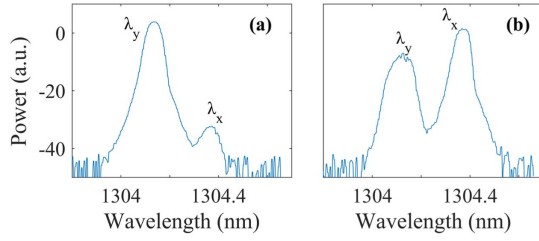
### A. Experimental Setup

Figure 1 shows the schematic diagram of the fiber-optic experimental setup. Two separate electrical signals are generated with a high-bandwidth arbitrary waveform generator (AWG, Keysight M8190a) representing the source image and the kernel used for the convolution process, respectively. These electrical signals (from Channels 1 and 2 of the AWG) are individually amplified by RF Amplifiers 1 and 2 before they are fed into two 10 GHz Mach–Zehnder (MZ) intensity modulators (Mod1 and Mod2) to encode the source image and



**Fig. 1.** Experimental setup of the binary convolution system based on a single VCSEL. TL, tunable laser; OI, optical isolator; VOA, variable optical attenuator; PC1, PC2, and PC3, polarization controllers; AWG, arbitrary waveform generator; Mod1, Mod2, Mach–Zehnder modulators; OC1, OC2, optical couplers; CIRC, circulator; Bias & T Controller, bias and temperature controller; PD, photodetector; PM, power meter; SCOPE, oscilloscope; OSA, optical spectrum analyzer.

kernel into an external optical signal. Compared with two paths of external optical injection, one external optical path, connecting two modulators, makes the injection locking of the VCSEL device easier. It also allows an easy approach to generate (in a single optical path) the required multi-level optical input signal. Additionally, using less optical devices reduces the energy consumption of the external optical path and reduces the cost of the photonic spiking neural network. The external optical signal is generated by a 1300 nm tunable laser (TL, Santec TLS-210 V). An optical isolator (OI) is included after the TL to avoid unwanted light reflections that might lead to spurious results. A variable optical attenuator (VOA) is used after the OI to adjust the strength of the light signal from the TL. The polarization of the optical signal from the TL is adjusted using three polarization controllers (PC1, PC2, and PC3), where PC1 and PC2 are specifically used to match the polarization of the optical signal to that which maximizes the performance of the two modulators, encoding, respectively, the image (Mod1) and the kernel (Mod2) information into the optical path. PC3 is used to adjust the final polarization of the encoded optical signal such that it matches the polarization of the targeted VCSEL mode. A 50:50 optical coupler (OC1) is used to split the light signal into two paths. The first one is connected to a power meter (PM) to monitor the input strength, whilst the second one is directly injected into a commercially available 1300 nm VCSEL through an optical circulator (CIRC). The output of the VCSEL, acting as a spiking optical neuron, is sent to an 8 GHz real-time oscilloscope (SCOPE, Rohde & Schwarz RTP) and an optical spectrum analyzer (OSA, Anritsu MS9710C) for analysis. The VCSEL was kept at a constant temperature of 293 K with an applied bias current of 6.5 mA (the lasing threshold current of the VCSEL was  $I_{th} = 2.96$  mA at 293 K). The optical spectrum of the free-running VCSEL is shown in Fig. 2(a), where the two lasing peaks correspond to the two orthogonal polarizations of the fundamental transverse mode of the device. We refer to the main lasing mode as the parallel polarized mode (or  $Y$ -polarized mode,  $Y_P$  mode,  $\lambda_y$ ) and to the subsidiary mode as the orthogonally polarized mode (or  $X$ -polarized mode,  $X_P$  mode,  $\lambda_x$ ). Figure 2(b) shows, in turn, the optical spectrum of the



**Fig. 2.** (a) Optical spectrum of free-running VCSEL used in the experiment. (b) Optical spectrum of the VCSEL subject to constant optical injection. Two polarization modes of VCSELs are referred to as  $\lambda_y$  (parallel) and  $\lambda_x$  (orthogonal).

1300 nm VCSEL device in the spiking regime, as it is subject to optical injection into the orthogonally polarized mode of the device. Upon injection of the external optical signal into the XP mode of the device, the XP mode becomes the dominant mode, whilst the YP mode becomes attenuated. The frequency detuning between the external optically injected signal and the XP mode of the VCSEL was equal to  $-5.64$  GHz. The power of the optically injected signal was  $127 \mu\text{W}$ .

### B. Theoretical Model

We use an extension of the well-known spin-flip model (SFM) to model the operation of the VCSEL acting as a spiking optical neuron. In our formulation, we add extra terms to the model's equations to account for the source image and kernel inputs. The rate equations can be described as follows [26,27]:

$$\begin{aligned} \frac{dE_{x,y}}{dt} = & -(k \pm \gamma_a)E_{x,y} - i(k\alpha \pm \gamma_p)E_{x,y} \\ & + k(1 + i\alpha)(NE_{x,y} \pm iE_{y,x}) \\ & + k_{\text{inj}}[E_{\text{inj}x1}(t) + E_{\text{inj}x2}(t)]e^{i\Delta\omega_x t} + F_{x,y}, \end{aligned} \quad (1)$$

$$\frac{dN}{dt} = -\gamma_N[N(1 + |E_x|^2 + |E_y|^2) - \mu + in(E_y E_x^* - E_x E_y^*)], \quad (2)$$

$$\frac{dn}{dt} = -\gamma_s n - \gamma_N[n(|E_x|^2 + |E_y|^2) + iN(E_y E_x^* - E_x E_y^*)], \quad (3)$$

where the subscripts  $x, y$  represent the XP and YP modes of the VCSEL, respectively.  $E_{x,y}$  is the slowly varying complex amplitude of the field in the XP and YP modes.  $N$  is the total carrier inversion between conduction and valence bands.  $n$  is the difference between carrier inversions with opposite spins.  $k$  denotes the field decay rate.  $\gamma_a$  and  $\gamma_p$  are the linear dichroism and the birefringence rate, respectively.  $\alpha$  is the linewidth enhancement factor.  $\gamma_N$  is the decay rate of  $N$ .  $\gamma_s$  is the spin-flip rate.  $\mu$  represents the normalized pump current.  $k_{\text{inj}}$  is the injected strength, and  $E_{\text{inj}x1}$  and  $E_{\text{inj}x2}$  indicate, respectively, the source image and kernel inputs.  $\Delta\omega_x$  is defined as  $\Delta\omega_x = \omega_{\text{inj}x} - \omega_0$ , where  $\omega_{\text{inj}x}$  is the angular frequency of the externally injected light in the XP mode, and  $\omega_0 = (\omega_x + \omega_y)/2$  is the center frequency between the XP and YP modes with

$\omega_x = \omega_0 + \alpha\gamma_a - \gamma_p$  and  $\omega_y = \omega_0 - \alpha\gamma_a + \gamma_p$ . The frequency detuning between the externally injected signal and the XP mode is set as  $\Delta f_x = f_{\text{inj}x} - f_x$ . Hence, in Eq. (1),  $\Delta\omega_x = 2\pi\Delta f_x + \alpha\gamma_a - \gamma_p$ .  $F_{x,y}$  are the spontaneous emission noise terms, which can be written as

$$F_x = \sqrt{\frac{\beta_{\text{sp}}\gamma_N}{2}} \left( \sqrt{N + n\xi_1} + \sqrt{N - n\xi_2} \right), \quad (4)$$

$$F_y = -i\sqrt{\frac{\beta_{\text{sp}}\gamma_N}{2}} \left( \sqrt{N + n\xi_1} - \sqrt{N - n\xi_2} \right), \quad (5)$$

where  $\beta_{\text{sp}}$  is the strength of the spontaneous emission, and  $\xi_1$  and  $\xi_2$  are independent complex Gaussian white noise terms of zero mean and a unit variance. We numerically solve Eqs. (1)–(4) using the fourth-order Runge–Kutta method. The parameter values configured for the 1300 nm VCSEL are as follows [27]:  $k = 185 \text{ ns}^{-1}$ ,  $\gamma_a = 2 \text{ ns}^{-1}$ ,  $\gamma_p = 128 \text{ ns}^{-1}$ ,  $\alpha = 2$ ,  $\gamma_N = 0.5 \text{ ns}^{-1}$ ,  $\gamma_s = 110 \text{ ns}^{-1}$ ,  $\beta_{\text{sp}} = 10^{-6}$ , and  $k_{\text{inj}} = 125 \text{ ns}^{-1}$ . With these parameters, the YP mode is the main lasing mode, and the XP mode is the subsidiary mode, as in Fig. 2(a).

## 3. EXPERIMENTAL AND NUMERICAL RESULTS

In this section, we firstly provide an experimental proof-of-concept demonstration of all-optical binary convolution with a spiking VCSEL neuron. We then calculate the image gradient magnitudes from a basic ‘‘Square’’ source image and a complex ‘‘Horse head’’ source image by means of all-optical binary convolution. Simulation results on the binary convolution and the calculation of image gradient magnitudes are also presented using a ‘‘Horse’’ source image from the latest version of the Berkeley Segmentation Data Set [32]. Finally, the robustness of our binary convolution system is also tested numerically by adding noise to the source image and kernel inputs.

### A. Experimental Results

Figure 3 shows an example of a binary two-dimensional (2D) convolution calculation, where a  $3 \times 3$  submatrix (9 pixels) from a source image and a kernel are element-wise multiplied, and the subsequent values of the multiplication are summated. In our experiment, we temporally encoded each pixel of the source image and the kernel inputs using rectangular pulses. Pixels of value ‘‘1’’ were optically encoded using intensity modulated power drops in the TL's light (via MZ modulators, Mod 1 and Mod 2), whereas pixels of value ‘‘0’’ produced no intensity modulation in the TL's light. The duration of each rectangular pulse encoding a pixel was set to  $1.5 \text{ ns}$  to match the refractory period of the experimentally measured spiking dynamics from the VCSEL neuron [17]. The experimental optical realization of the binary convolution example provided in Fig. 3 is depicted graphically in Fig. 4. Figures 4(a) and 4(b) plot, respectively, the temporally encoded 9 pixel ( $3 \times 3$ ) image submatrix and kernel inputs generated for the example given in Fig. 3. Given that the optically encoded source image and kernel inputs were injected into the VCSEL synchronously, we delayed the kernel input such that its modulation (in Mod 2) occurred on top of the corresponding modulated image

$$\begin{array}{|c|c|c|} \hline 1 & 0 & 0 \\ \hline 0 & 1 & 1 \\ \hline 1 & 1 & 0 \\ \hline \end{array} \otimes \begin{array}{|c|c|c|} \hline 1 & 0 & 1 \\ \hline 1 & 1 & 1 \\ \hline 0 & 1 & 1 \\ \hline \end{array} = 4$$

Image                      Kernel

**Fig. 3.** Example of a single step during a 2D binary convolution operation. During this step, a Hadamard (element-wise) product is calculated for a submatrix of the image and the kernel, and all of the values in the multiplication result are summed up to obtain a single value.

input (from Mod 1). We introduced a delay time in the kernel input (directly using the AWG) equal to the time required for a light pulse to travel from Mod 1 to Mod 2. Figure 4(c) shows the optical signal measured after Mod 2 in the setup, combining in a single input line the temporal image and kernel information given in Figs. 4(a) and 4(b). This signal, which was injected into the VCSEL neuron to perform the binary convolution had three different levels (low, medium, and high) depending on the specific pixel values in the image and kernel at a given instance. We control the conditions of the injected signal [in Fig. 4(c)] in such a way that the medium and high input levels injection lock the VCSEL to the external signal, delivering a constant stable temporal output. The lowest input level brings the VCSEL out of the injection locking and into a dynamical region, where the device produces fast spiking dynamical responses [24]. Figure 4(d) shows the experimentally measured time series at the VCSEL neuron's output, yielding stable or spiking outputs depending on the input intensity levels [from Fig. 4(c)]. Importantly, Fig. 4(d) shows that the number of spikes fired by the VCSEL neuron directly provides the result of the binary convolution. It can be seen in Fig. 4(d) that four fast (<100 ps long) spikes are fired by the VCSEL neuron, the same result as that of the binary convolution example in Fig. 3.

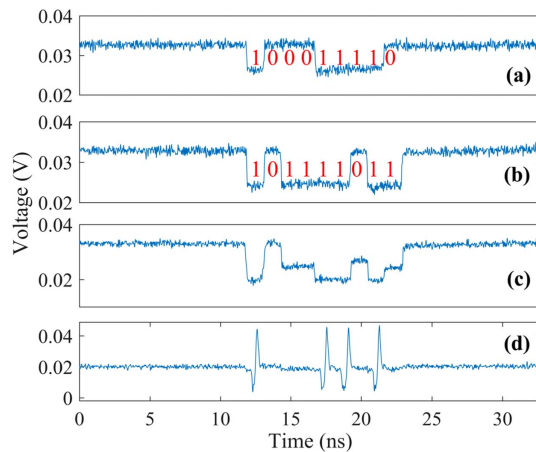


**Fig. 4.** Experimental convolution operation. (a) Inputs of Channel 1 (image in Fig. 3). (b) Inputs of Channel 2 (kernel in Fig. 3). (c) Inputs of VCSEL. (d) Outputs of VCSEL (the results of convolution).

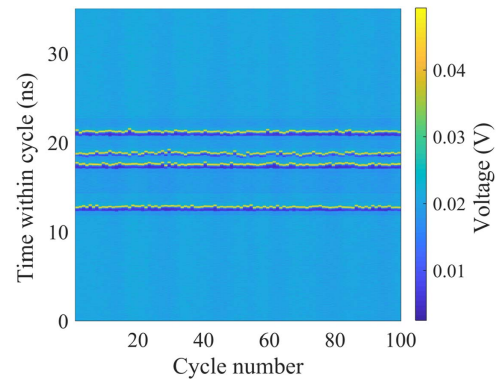


**Fig. 5.** Temporal map of 100 superimposed consecutive convolutional results measured experimentally at the output of spiking VCSEL neuron.

Figure 5 shows a temporal map [17] merging in a single plot 100 superimposed consecutive convolutional outputs from the photonic spiking VCSEL neuron. The image and kernel inputs and the experimental conditions are the same as those shown in Fig. 4. Spike events are depicted in yellow in the color map of Fig. 5, and steady state responses appear in light blue. Figure 5 clearly shows that binary convolutional results to 100 consecutive inputs remain the same, producing, in all 100 cases, four separate spiking responses at the VCSEL's output. The optical binary convolutional results obtained with the spiking VCSEL neuron are, therefore, consistent and reproducible. This proof-of-concept result obtained with a spiking VCSEL highlights a new, controllable way to perform convolution operations for information and image processing tasks.

## B. Calculation of Image Gradient Magnitudes

In this section, the image gradient magnitude, critical to image edge detection, is calculated using our approach based on a single spiking VCSEL neuron and optical binary convolution. The image gradient magnitude  $G(x)$  of a given pixel  $x$  is calculated using the following equations [33]:

$$G(x) = \sqrt{G_X(x)^2 + G_Y(x)^2}, \quad (6)$$

$$G_X(x) = [B(x) \otimes B_X^+] - [B(x) \otimes B_X^-], \quad (7)$$

$$G_Y(x) = [B(x) \otimes B_Y^+] - [B(x) \otimes B_Y^-]. \quad (8)$$

Four binary convolutions, i.e.,  $B(x) \otimes B_{X,Y}^\pm$ , are used in  $G_X(x)$  and  $G_Y(x)$ .  $B(x) = \sum_{p=0}^{N-1} s(i_p, i_x) \cdot 2^p$  is the  $N$  bit local binary pattern descriptor of pixel  $x$ .  $i_x$  is the central pixel intensity, and  $i_p$  is the intensity of the  $p$ th neighbor of  $x$  in the source pattern. The comparison operator is defined as

$$s(i_p, i_x) = \begin{cases} 1 & \text{if } |i_p - i_x| > T_x, \\ 0 & \text{otherwise} \end{cases}, \quad (9)$$

where  $T_x = \frac{1}{4} i_x + 20$  and  $N = 5 \times 5 - 1$ .

The range of the local binary pattern descriptor of a pixel is presented in gray color in Fig. 6(a). In Fig. 6(b), a "Square" source image is made up of a solid black  $10 \times 10$  pixels square

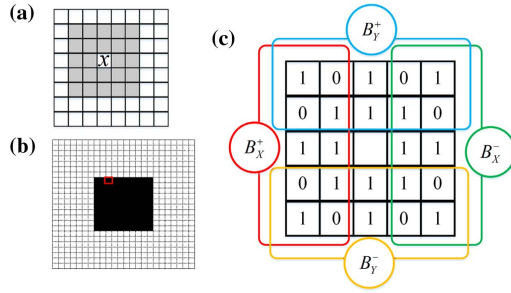


**Fig. 6.** (a) Gray color: range of the local binary pattern descriptor of pixels. (b) A  $24 \times 24$  pixels “Square” source image. The red highlight indicates a given pixel in the image. (c) The four convolutions ( $B_X^+$ ,  $B_X^-$ ,  $B_Y^+$ , and  $B_Y^-$ ) of the  $5 \times 5$  binary pattern. Bits that fall outside the highlighted areas for a given string are set to zero.

on a  $24 \times 24$  pixels white background. In the grayscale image, the intensities of white and black pixels are 255 and 0, respectively. For example, the intensity of the red-highlighted pixel  $x$  in Fig. 6(b) is  $i_x = 255$ . We arrange and serialize the pixels in the range of local binary pattern descriptors by columns. The first neighbor pixel intensity is  $i_1 = 0$ ; hence, according to Eq. (9),  $s(i_1, i_x) = 1$ . The third neighbor is  $i_3 = 255$ ; hence,  $s(i_3, i_x) = 0$ .  $B(x)$  can be calculated for the red-highlighted pixel in Fig. 6(b) as follows:

$$B(x) = \begin{bmatrix} s(i_1, i_x) & - & - & - & s(i_{20}, i_x) \\ s(i_2, i_x) & - & - & - & s(i_{21}, i_x) \\ s(i_3, i_x) & - & x & - & s(i_{22}, i_x) \\ s(i_4, i_x) & - & - & - & s(i_{23}, i_x) \\ s(i_5, i_x) & - & - & - & s(i_{24}, i_x) \end{bmatrix} \\ = \begin{bmatrix} 1 & 1 & 1 & 1 & 1 \\ 1 & 1 & 1 & 1 & 1 \\ 0 & 0 & x & 0 & 0 \\ 0 & 0 & 0 & 0 & 0 \\ 0 & 0 & 0 & 0 & 0 \end{bmatrix}. \quad (10)$$

For the red-highlighted pixel  $x$  in Fig. 6(b), “1” in  $B(x)$  corresponds to a white pixel, and “0” corresponds to a black pixel in the source image.

In Eqs. (7) and (8),  $B_X^+$ ,  $B_X^-$ ,  $B_Y^+$ , and  $B_Y^-$  are the four kernels that are adopted as in Ref. [33]. Figure 6(c) shows the areas of the four different kernels. Pixels that fall outside of the highlighted areas in Fig. 6(c) for a given string are set to zero. For example,

$$B_X^+ = \begin{bmatrix} 1 & 0 & 0 & 0 & 0 \\ 0 & 1 & 0 & 0 & 0 \\ 1 & 1 & 0 & 0 & 0 \\ 0 & 1 & 0 & 0 & 0 \\ 1 & 0 & 0 & 0 & 0 \end{bmatrix}. \quad (11)$$

We arrange and serialize the pixels of  $B(x)$  and the four kernels by columns. For example, the string of  $B(x)$  is [1, 1, 0, 0, 0, 0, 1, 1, 0, 0, 0, 0...], and the string of  $B_X^+$  is [1, 0, 1, 0, 1, 0, 1, 1, 1, 0...]. We studied experimentally the response of the VCSEL

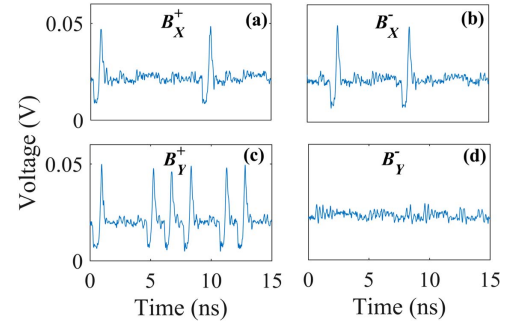


**Fig. 7.** Four convolutional results with four highlighted area kernels for one pixel, which has red box in Fig. 6.

neuron under the injection of the “Square” source image and kernel operators included in Figs. 6(b) and 6(c). Specifically, Fig. 7 showcases the experimentally recorded results at the VCSEL output for each kernel when operating on the red-highlighted pixel in Fig. 6(b). It can be seen in Fig. 7(a) that fast [sub-nanosecond (ns)] spikes are only triggered by the 1st and 7th pixels. Therefore, the convolutional result for  $B(x) \otimes B_X^+$  is two, as was expected. Here, the convolutional result is measured offline, where the number of spiking responses is counted using software. This could be achieved in future realizations experimentally using electronic or photonic spike/photon counting hardware. Similarly, from Figs. 7(b)–7(d) we can see that 2, 6, and 0 sub-ns spikes are elicited at the VCSEL’s output for kernels  $B_X^-$ ,  $B_Y^+$ , and  $B_Y^-$ , respectively. Using the experimental results measured from the spiking VCSEL neuron, we calculate off-line  $G_X(x)$ ,  $G_Y(x)$ , and  $G(x)$  to determine the image gradient magnitude. Based on the experimentally measured results in Figs. 7(a)–7(d),  $G_X(x)$ ,  $G_Y(x)$ , and  $G(x)$  are 0, 6, and 6, respectively, using Eqs. (7)–(9).

The experimental process in Fig. 7 is repeated consecutively for every single pixel in the “Square” source image [Fig. 6(b)] to calculate their image gradient magnitudes. The latter are used to build the reconstructed image in Fig. 8(a), providing a gradient map for the “Square” source image. Figure 8(a) clearly reveals a “hollow” square shape in the experimentally produced gradient map, hence, detecting all edge features of the source image. Here, the corner and edge pixels are omitted [34]. In Fig. 8(a), the pixels with a gradient magnitude  $G(x) > 3$  can be selected to thin the response and reveal the true edges

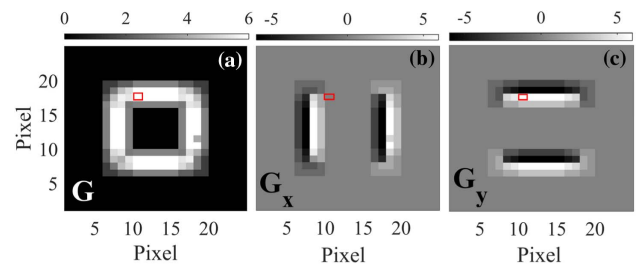


**Fig. 8.** Gradient maps of the “Square” source image. Visualizations of (a)  $G$ , (b)  $G_X$ , and (c)  $G_Y$  maps of the “Square” source image based on the optical binary convolution performed by the VCSEL neuron.

of the “Square” [33,35]. Additionally, Figs. 8(b) and 8(c) plot separately the reconstructed images using the obtained values for  $G_X(x)$  and  $G_Y(x)$  from the experimentally measured time series at the VCSEL neuron’s output. Figures 8(b) and 8(c) reveal that both vertical and horizontal lines can be individually detected from the source image in Fig. 6(b) using, respectively, the magnitudes  $G_X(x)$  and  $G_Y(x)$ . For one pixel  $x$ , a total of 15 ns is required to process each of the four binary convolutions, as shown in Fig. 7. Hence, 60 ns (15 ns  $\times$  4) is needed for the binary convolutions of one pixel with our single VCSEL system. The time required for binary convolution is, therefore, dependent on the number of pixels in the image. Considering that the optical power of the VCSEL is on average equal to  $\sim 500$   $\mu$ W, for the different operation conditions used in this work, we can estimate the energy consumption of the binary convolution for one pixel as 30 pJ (0.5 mW  $\times$  60 ns) in our system. In the future, the binary convolution operation could be achieved using multiple devices integrated in a VCSEL array simultaneously. Such a new architecture would increase the speed of the convolution operation, obviously at the expense of increasing the system’s complexity. This work therefore provides a low complexity, reduced energy consumption, and fast hardware approach for photonic binary convolution for novel light-enabled image processing functionalities.

To further investigate our experimental system, we focused on demonstrating the achievement of gradient maps from a complex source image using the all-optical binary convolution of this work, as seen in Fig. 9. For this purpose, we selected as a source image for our VCSEL-based binary convolution system a complex “Horse head” image [Fig. 9(b)]. This is a  $100 \times 105$

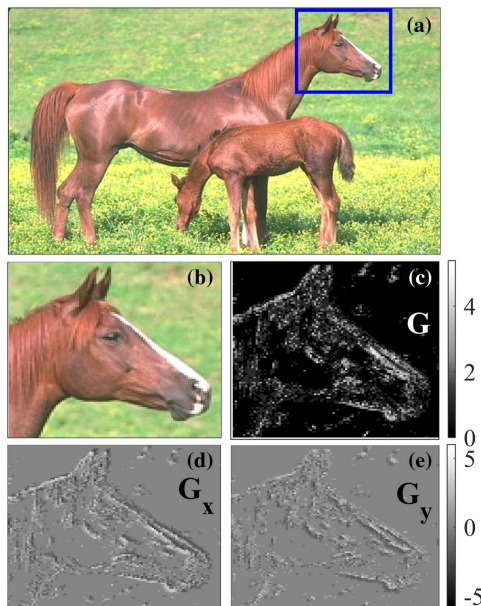


**Fig. 9.** “Horse head” image and the gradient maps of the “Horse head” image. (a) Source “Horse” image. The blue box indicates the “Horse Head” image used for analysis in (b). Visualizations of the (c)  $G$ , (d)  $G_X$ , and (e)  $G_Y$  maps of the “Horse head” image obtained from the optical binary convolution performed with the VCSEL neuron.

pixels portion of the “Horse” image from the Berkeley Segmentation Data Set [32] [also included in Fig. 9(a)]. The color image was converted to grayscale before we applied the same experimental methods used previously to obtain the results included in Fig. 8 above. The values of  $G(x)$ ,  $G_X(x)$ , and  $G_Y(x)$  experimentally achieved for the complex “Horse head” image [Fig. 9(b)] are shown in Figs. 9(c)–9(e), respectively. These gradient maps reveal the successful detection of the edge features in this complex image, hence permitting the successful recreation of the outline and shape of the horse head. This effectively demonstrates that the reported all-optical binary convolution technique with a VCSEL neuron is also suitable for complex high-resolution source images.

### C. Numerical Results

In this section, binary convolution based on a single VCSEL neuron is performed numerically. The robustness of the system to perform all-optical binary convolution under noisy inputs and for larger kernels is investigated. Finally, the calculation of image gradient magnitudes with our photonic approach using a single VCSEL neuron is presented numerically using the “Horse” image from the latest version of the Berkeley Segmentation Data Set [32].

The binary convolution example given in Fig. 3 and experimentally performed with the VCSEL neuron (see Fig. 4) is numerically simulated using the SFM model in Figs. 10(a1)–10(c1). Pixels of value “1” are numerically implemented using power drop pulses with a strength  $K_p = 0.852$  ( $K_p =$  pulse power/constant power) and a duration of 1.5 ns (as in the experimental demonstration). The frequency detuning between the externally injected signal and the XP mode in the VCSEL model is set to  $-3.66$  GHz. Figures 10(a1)–10(c1) plot the numerically obtained results for the all-optical binary convolution with a VCSEL neuron. Specifically, Figs. 10(a1) and 10(b1) plot, respectively, the time series for the temporally encoded image [Fig. 10(a1)] and kernel [Fig. 10(b1)] inputs, whilst Fig. 10(c1) plots the numerically calculated output from the VCSEL neuron. The latter clearly shows that the simulation successfully reproduces the

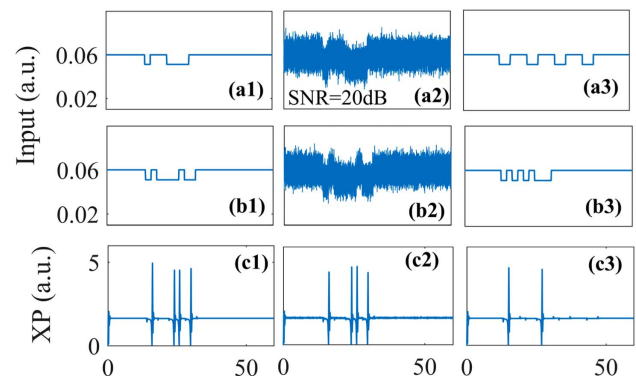


**Fig. 10.** (a1)–(a3) Inputs of Channel 1 (image in Fig. 3). (b1)–(b3) Inputs of Channel 2 (kernel in Fig. 3). (c1)–(c3) VCSEL neuron’s output. (a1)–(c1) Convolutional operation in the VCSEL neuron without noise. (a2)–(c2) Convolutional operation in the VCSEL neuron with added input noise of SNR = 20 dB. (a3)–(c3) Convolution operation with a  $5 \times 5$  pixels kernel.

outcome of the experimental all-optical binary convolution [see Fig. 4(d)], where four spikes are elicited by the VCSEL. This excellent agreement between the modeled results and the experimental findings gives us confidence to test the robustness of the photonic binary convolution system under the injection of inputs with added noise. To study this aspect, we model the response of the VCSEL binary convolutional system under the injection of noisy inputs with a configured SNR = 20 dB [see results in Figs. 10(a2) and 10(b2)]. Specifically, Fig. 10(c2) shows that the exact same response is obtained from the VCSEL neuron as compared to the case with no added noise in Fig. 10(c1). This outlines the robustness to noise of the proposed all-optical VCSEL convolutional system. Additionally, the numerical convolution with a larger  $5 \times 5$  pixels kernel is tested numerically in Figs. 10(a3)–10(c3) using Eq. (10) and Eq. (11) as inputs. Figure 10(c3) shows that the modeled convolutional result obtained from the VCSEL neuron also produces two fast spike events, hence yielding the exact same outcome as obtained experimentally in Fig. 7(a). We can therefore deduce that the convolution results that can be obtained with our VCSEL-neuron-based approach are not limited by the dimension of the kernel operators or the resolution of the image.

Figure 11 shows the numerically calculated gradient maps obtained with a spiking VCSEL neuron for the “Horse” source image [32] with a resolution of  $481 \times 321$  pixels [Figs. 11(a) and 9(a)]. Figures 11(b)–11(d) show the calculated gradient maps for  $G(x)$ ,  $G_X(x)$ , and  $G_Y(x)$ , respectively. These were obtained using the  $5 \times 5$  kernel introduced in the experimental study of the “Square” source image (see Figs. 6–8). It can be seen that the numerical simulation successfully reveals the image edge information through the gradient magnitude  $G(x)$ , as seen in Fig. 11(b), as well as the individual horizontal and vertical edge features of the source image through  $G_X(x)$  and  $G_Y(x)$ , as seen in Figs. 11(c) and 11(d), respectively. These results, showing good overall agreement with the experimental findings of Fig. 9, therefore numerically validate that the gradient magnitude can be successfully calculated with a

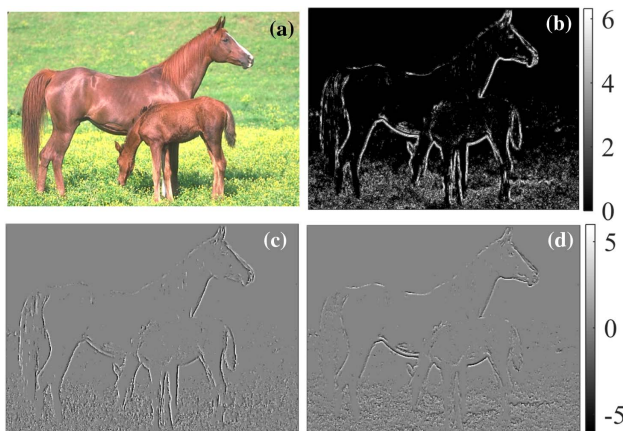


**Fig. 11.** “Horse” image and gradient maps of the “Horse” image. (a) “Horse” image. Visualizations of (b)  $G$ , (c)  $G_X$ , and (d)  $G_Y$  maps of “Horse” image based on the numerical optical binary convolution in VCSEL.

photonic spiking VCSEL neuron, irrespective of the image dimensionality.

Optical binary convolution can be used in systems where simplified convolutional operations, with binary inputs (still able to provide high-performance accuracy), provide other key advantages in terms of increased operation speed, lowered energy consumption, and reduced hardware requirements. This is the case of the system reported in this work, using an extremely hardware friendly implementation of a single VCSEL to perform high-speed and low energy (<pJ/spike) image edge-feature detection. Besides, in our approach, the results of the binary convolution are output in an optical spiking representation, providing unique advantages in terms of robustness to noise and high precision of convolutional results. This spiking representation therefore enables our platform to successfully perform with noisy optical and electronic signals. Whilst other recent works have recently reported complex systems for optical convolution operation using temporally modulated inputs and weights for image processing tasks showing excellent performance [36], our technique benefits from an extremely simple architecture using just one off-the-shelf, inexpensive 1300 nm VCSEL to perform the binary convolution operation for image edge-feature detection. Our approach combining a VCSEL-based spiking photonic neuron with time multiplexing is able to deliver the operation of a full neuronal layer, where each 1.5-ns-long time slot operates in fact as a virtual neuron (or node) processing specific image pixel information. This offers great promise for future implementation of interconnected VCSEL-based neuronal network architectures for image processing tasks of increased complexity (e.g., image classification) and using neuron-like spiking signals to operate.

The utilization of binary convolution in the calculation of image gradient maps has been reported to outperform the alternative Canny implementation [35] of image gradient maps convolution, in the Intel i7 mobile processor [33]. In that report, the frequency of the binary gradient-based edge detector was 4.7 Hz, while the Canny convolution approach was found to operate at 0.5 Hz. This indicates that binary convolution can be performed at speeds faster than alternative convolution approaches. Additionally, mobile processors operate with powers of several watts (for example, the Intel i7 has a power of 15 W) [37], whilst VCSELs, such as the one used in this work, provide low power performance typically at milliwatt (mW) and sub-mW power levels. Hence, the energy consumption for the calculation of image gradient maps obtained with our VCSEL-based optical binary convolution system can be significantly more energy efficient, as well as yield faster operation speeds, than the performance achieved with traditional or binary convolution methods in digital processors.

#### 4. CONCLUSION

In this work, we proposed and investigated experimentally and numerically an all-optical binary convolution system using a VCSEL operating as a photonic spiking neuron. The inputs (image and kernel) are encoded temporally using fast rectangular pulses (1.5-ns-long) and optically injected into the VCSEL neuron. The latter’s optical output directly provides the results of the convolution in the number of (sub-ns long) spikes fired.

In addition to performing all-optical binary convolution, we demonstrated experimentally and numerically the ability of the proposed system to calculate the image gradient magnitudes from digital source images. This feature was successfully used to identify key edge features from a source image as well as its separate horizontal and vertical components. Furthermore, we investigated numerically the robustness of the proposed VCSEL-based convolutional system to input noise. This simple system, using a single commercially available VCSEL operating at the key telecom wavelength of 1300 nm, offers a novel photonic solution to binary convolution with the advantage of being highly energy efficient and hardware friendly. This opens exciting prospects for a new photonic spiking platform for future optical binary spiking CNNs. Furthermore, the high-speed, low cost, and neuronal functionalities of these photonic spiking systems hold promise for numerous processing tasks expanding into fields such as computer vision and artificial intelligence.

**Funding.** UKRI Turing AI Acceleration Fellowships Programme (EP/V025198/1); Office of Naval Research Global (ONRGNICOP-N62909-18-1-2027); European Commission (828841-ChipAI-H2020-FETOPEN2018-2020); UK's EPSRC Doctoral Training Partnership (EP/N509760); National Natural Science Foundation of China (61674119, 61974177); China Scholarship Council.

**Acknowledgment.** We thank Prof. T. Ackemann and Prof. A. Kemp (University of Strathclyde) for lending some of the equipment used in this work. All data underpinning this publication are openly available from the University of Strathclyde KnowledgeBase at <https://doi.org/10.15129/51af27bc-8cc2-46a7-9088-1aad87e4340c>.

**Disclosures.** The authors declare no conflicts of interest.

## REFERENCES

- O. Abdel-Hamid, A. R. Mohamed, H. Jiang, and G. Penn, "Applying convolutional neural networks concepts to hybrid NN-HMM model for speech recognition," in *IEEE International Conference on Acoustics, Speech and Signal Processing (ICASSP)* (2012), pp. 4277–4280.
- J. Fu, H. Zheng, and T. Mei, "Look closer to see better: recurrent attention convolutional neural network for fine-grained image recognition," in *Proceedings of the IEEE Conference on Computer Vision and Pattern Recognition* (2017), pp. 4438–4446.
- K. Gopalakrishnan, S. K. Khaitan, A. Choudhary, and A. Agrawal, "Deep convolutional neural networks with transfer learning for computer vision-based data-driven pavement distress detection," *Constr. Build. Mater.* **157**, 322–330 (2017).
- P. Y. Simard, D. Steinkraus, and J. C. Platt, "Best practices for convolutional neural networks applied to visual document analysis," in *International Conference on Document Analysis and Recognition (ICDAR)* (2003), pp. 958–963.
- C. Farabet, C. Couprie, L. Najman, and Y. LeCun, "Learning hierarchical features for scene labeling," *IEEE Trans. Pattern Anal. Mach. Intell.* **35**, 1915–1929 (2013).
- L. Cavigelli, M. Magno, and L. Benini, "Accelerating real-time embedded scene labeling with convolutional networks," in *Proceedings of the 52nd Annual Design Automation Conference* (2015), paper 108.
- M. Rastegari, V. Ordonez, J. Redmon, and A. Farhadi, "Xnor-net: ImageNet classification using binary convolutional neural networks," in *European Conference on Computer Vision (ECCV)* (2016), pp. 525–542.
- F. Juefei-Xu, V. N. Boddeti, and M. Savvides, "Local binary convolutional neural networks," in *Proceedings of the IEEE Conference on Computer Vision and Pattern Recognition* (2017), pp. 19–28.
- X. Lin, C. Zhao, and W. Pan, "Towards accurate binary convolutional neural network," in *Advances in Neural Information Processing Systems (NIPS)* (2017), pp. 345–353.
- M. Courbariaux, Y. Bengio, and J.-P. David, "BinaryConnect: training deep neural networks with binary weights during propagations," in *Advances in Neural Information Processing Systems (NIPS)* (2015), pp. 3105–3113.
- M. Courbariaux, I. Hubara, D. Soudry, R. El-Yaniv, and Y. Bengio, "Binarized neural networks: training deep neural networks with weights and activations constrained to +1 or -1," arXiv:1602.02830 (2016).
- M. Turconi, B. Garbin, M. Feyereisen, M. Giudici, and S. Barland, "Control of excitable pulses in an injection-locked semiconductor laser," *Phys. Rev. E* **88**, 022923 (2013).
- P. R. Prucnal, B. J. Shastri, T. F. de Lima, M. A. Nahmias, and A. N. Tait, "Recent progress in semiconductor excitable lasers for photonic spike processing," *Adv. Opt. Photon.* **8**, 228–299 (2016).
- S. Xiang, Y. Zhang, J. Gong, X. Guo, L. Lin, and Y. Hao, "STDP-based unsupervised spike pattern learning in a photonic spiking neural network with VCSELs and VCSOs," *IEEE J. Sel. Top. Quantum Electron.* **25**, 1700109 (2019).
- Y. Zhang, S. Xiang, X. Guo, A. Wen, and Y. Hao, "All-optical inhibitory dynamics in photonic neuron based on polarization mode competition in a VCSEL with an embedded saturable absorber," *Opt. Lett.* **44**, 1548–1551 (2019).
- J. Feldmann, N. Youngblood, C. D. Wright, H. Bhaskaran, and W. H. P. Pernice, "All-optical spiking neurosynaptic networks with self-learning capabilities," *Nature* **569**, 208–214 (2019).
- J. Robertson, E. Wade, Y. Kopp, J. Bueno, and A. Hurtado, "Toward neuromorphic photonic networks of ultrafast spiking laser neurons," *IEEE J. Sel. Top. Quantum Electron.* **26**, 7700715 (2019).
- A. Mehrabian, Y. Al-Kabani, V. J. Sorger, and T. El-Ghazawi, "PCNNA: a photonic convolutional neural network accelerator," in *IEEE International System-on-Chip Conference (SOCC)* (2018), pp. 169–173.
- H. Bagherian, S. Skirlo, Y. Shen, H. Meng, V. Ceperic, and M. Soljagic, "On-chip optical convolutional neural networks," arXiv:1808.03303 (2018).
- S. Xu, J. Wang, R. Wang, J. Chen, and W. Zou, "High-accuracy optical convolution unit architecture for convolutional neural networks by cascaded acousto-optical modulator arrays," *Opt. Express* **27**, 19778–19787 (2019).
- S. Xu, J. Wang, and W. Zou, "High-energy-efficiency integrated photonic convolutional neural networks," arXiv:1910.12635 (2019).
- K. Iga and H. E. Li, *Vertical-Cavity Surface-Emitting Laser Devices* (Springer, 2003).
- R. Michalzik, *VCSELs: Fundamentals, Technology and Applications of Vertical-Cavity Surface-Emitting Lasers*, Springer Series in Optical Sciences (Springer-Verlag, 2013), Vol. **166**.
- A. Hurtado and J. Javaloyes, "Controllable spiking patterns in long-wavelength vertical cavity surface emitting lasers for neuromorphic photonics systems," *Appl. Phys. Lett.* **107**, 241103 (2015).
- B. Garbin, J. Javaloyes, G. Tissoni, and S. Barland, "Topological solitons as addressable phase bits in a driven laser," *Nat. Commun.* **6**, 5915 (2015).
- S. Y. Xiang, A. J. Wen, and W. Pan, "Emulation of spiking response and spiking frequency property in VCSEL-based photonic neuron," *IEEE Photon. J.* **8**, 1504109 (2016).
- T. Deng, J. Robertson, and A. Hurtado, "Controlled propagation of spiking dynamics in vertical-cavity surface-emitting lasers: towards neuromorphic photonic networks," *IEEE J. Sel. Top. Quantum Electron.* **23**, 1800408 (2017).
- J. Robertson, T. Deng, J. Javaloyes, and A. Hurtado, "Controlled inhibition of spiking dynamics in VCSELs for neuromorphic photonics: theory and experiments," *Opt. Lett.* **42**, 1560–1563 (2017).



29. A. Dolcemascolo, B. Garbin, B. Peyce, R. Veltz, and S. Barland, "Resonator neuron and triggering multipulse excitability in laser with injected signal," *Phys. Rev. E* **98**, 062211 (2018).
30. J. Robertson, M. Hejda, J. Bueno, and A. Hurtado, "Ultrafast optical integration and pattern classification for neuromorphic photonics based on spiking VCSEL neurons," *Sci. Rep.* **10**, 1 (2020).
31. M. Hejda, J. Robertson, J. Bueno, and A. Hurtado, "Spike-based information encoding in VCSELs for neuromorphic photonic systems," *J. Phys.* **2**, 044001 (2020).
32. P. Arbelaez, M. Maire, C. Fowlkes, and J. Malik, "Contour detection and hierarchical image segmentation," *IEEE Trans. Pattern Anal. Mach. Intell.* **33**, 898–916 (2011).
33. P. L. St-Charles, G. A. Bilodeau, and R. Bergevin, "Fast image gradients using binary feature convolutions," in *Proceedings of the IEEE Conference on Computer Vision and Pattern Recognition* (2016), pp.1–9.
34. E. Nadernejad, "Edge detection techniques: evaluations and comparisons," *Appl. Math. Sci.* **2**, 1507–1520 (2008).
35. J. Canny, "A computational approach to edge detection," *IEEE Trans. Pattern Anal. Mach. Intell.* **8**, 679–698 (1986).
36. R. Hamerly, L. Bernstein, A. Sludds, M. Soljačić, and D. Englund, "Large-scale optical neural networks based on photoelectric multiplication," *Phys. Rev. X* **9**, 021032 (2019).
37. V. Spiliopoulos, G. Keramidas, S. Kaxiras, and K. Efstathiou, "Power-performance adaptation in Inter core i7," in *Proceedings of 2nd Workshop Computer Architecture and Operating System Co-design* (2011), pp. 1–10.